JGR Space Physics

RESEARCH ARTICLE
10.1029/2022JA031136

Multi-Instrument Observations of the Effects of a Solar Wind Pressure Pulse on the High Latitude Ionosphere: A Detailed Case Study of a Geomagnetic Sudden Impulse

A. R. Fogg[1,2], M. Lester[1], T. K. Yeoman[1], J. A. Carter[1], S. E. Milan[1], H. K. Sangha[1,3], T. Elsden[4], S. J. Wharton[1], M. K. James[1], J. Malone-Leigh[2,5], L. J. Paxton[6], B. J. Anderson[6], and S. K. Vines[6]

[1]School of Physics and Astronomy, University of Leicester, Leicester, UK, [2]School of Cosmic Physics, DIAS Dunsink Observatory, Dublin Institute for Advanced Studies, Dublin 15, Ireland, [3]The Center for Space Plasma and Aeronomic Research (CSPAR), The University of Alabama in Huntsville, Huntsville, AL, USA, [4]School of Mathematics and Statistics, University of St Andrews, St Andrews, UK, [5]Trinity College Dublin, Dublin, Ireland, [6]John Hopkins University Applied Physics Laboratory, Laurel, MD, USA

Key Points:

- A positive sudden impulse (SI) is observed on 16 June 2012 at 20:19 UT in SYM-H
- A superposition of Alfvén and compressional propagation modes are observed in magnetometer data
- Collocated lobe reconnection vortices and region 0 field aligned currents are enhanced by the SI

Correspondence to:

A. R. Fogg,
arfogg@cp.dias.ie

Citation:

Fogg, A. R., Lester, M., Yeoman, T. K., Carter, J. A., Milan, S. E., Sangha, H. K., et al. (2023). Multi-instrument observations of the effects of a solar wind pressure pulse on the high latitude ionosphere: A detailed case study of a geomagnetic sudden impulse. *Journal of Geophysical Research: Space Physics*, *128*, e2022JA031136. https://doi.org/10.1029/2022JA031136

Received 3 NOV 2022
Accepted 3 MAR 2023

Abstract The effects of a solar wind pressure pulse on the terrestrial magnetosphere have been observed in detail across multiple datasets. The communication of these effects into the magnetosphere is known as a positive geomagnetic sudden impulse (+SI), and are observed across latitudes and different phenomena to characterize the propagation of +SI effects through the magnetosphere. A superposition of Alfvén and compressional propagation modes are observed in magnetometer signatures, with the dominance of these signatures varying with latitude. For the first time, collocated lobe reconnection convection vortices and region 0 field aligned currents are observed preceding the +SI onset, and an enhancement of these signatures is observed as a result of +SI effects. Finally, cusp auroral emission is observed collocated with the convection and current signatures. For the first time, simultaneous observations across multiple phenomena are presented to confirm models of +SI propagation presented previously.

1. Introduction

The terrestrial magnetosphere-ionosphere system is strongly coupled to the solar wind, which is highly variable on short timescales. Near-step changes in solar wind dynamic pressure, known as pressure pulses which when positive, can rapidly excite and restructure the electrodynamics within the magnetosphere-ionosphere system. When the effects of a rapid change in solar wind dynamic pressure are communicated into the magnetosphere, this is known as a geomagnetic sudden commencement (SC, Araki, 1994), indicated by a corresponding step change in the ring current index SYM-H (e.g., Hori et al., 2015; Takeuchi et al., 2002). SCs can be further subdivided into two categories: sudden impulses (SIs) and sudden storm commencements (SSCs). Although the definition of these three terms (SC, SI and SSC) is not always consistent in the literature, in this paper an SSC is defined as an SC which is rapidly (within 12 hr (Taylor et al., 1994)) followed by a geomagnetic storm, otherwise it is an SI.

The majority of pressure pulses observed in the solar wind are caused by dramatic phenomena such as coronal mass ejections (CMEs) or corotating interaction regions (CIRS, e.g., Zuo et al., 2015). CMEs are violent eruptions of plasma from the Sun, resulting from magnetic reconnection (e.g., Hundhausen, 1995) and can cause SSCs (Taylor et al., 1994). CIRs, also called fast-slow stream interaction regions, have steep pressure gradients resulting from fast flowing plasma catching up with more slowly rotating plasma on more tightly wound magnetic field lines (e.g., Hundhausen, 1995). CIRs can cause Storm Gradual Commencements (SGCs, Taylor et al., 1994), which are geomagnetic storms not related to an SC. If there is no subsequent storm, a positive SI (+SI) may result from an increase in pressure, and a negative SI (−SI) may result from a decrease in pressure. An SI is generally considered to be driven by a pressure change of at least 3 nPa in under 10 min (e.g., Coco et al., 2011), although it can also be identified with SYM-H (e.g., Hori et al., 2015). Hori et al. (2015) define the SC signature in SYM-H as an increase of more than 5 nT with a gradient greater than about 15 nT per 10 s. Given the magnitude of the pressure change, SIs can have a remarkably dramatic impact on the Earth's magnetosphere, and the electrodynamics within.

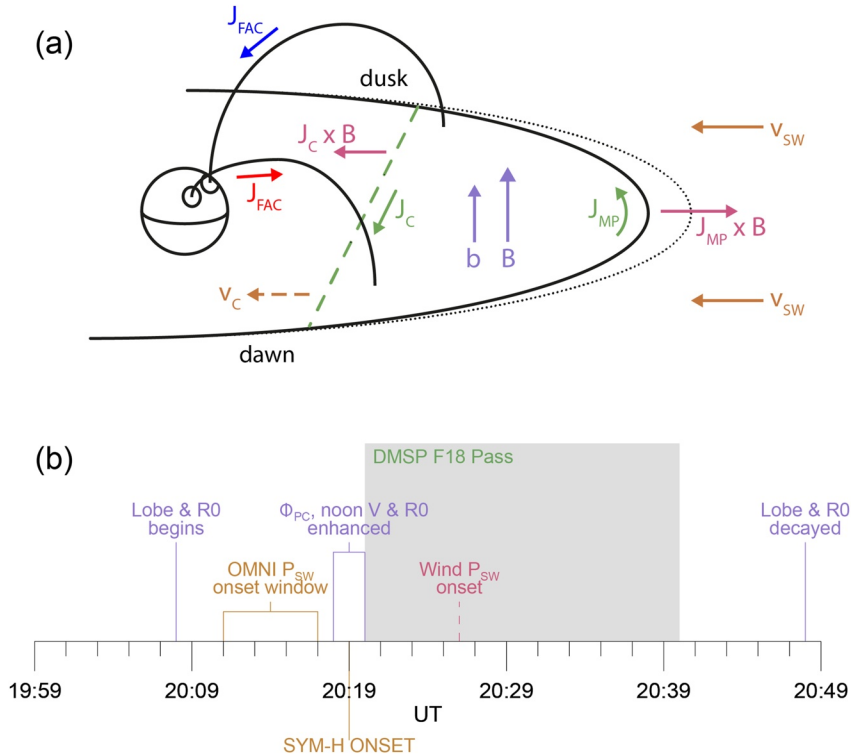

Figure 1. (a) Schematic showing the effects and propagation of a sudden impulse (SI) into the terrestrial magnetosphere (dayside on the right), after Figure 12d of Araki (1994). The magnetopause before (after) the compression is drawn in as a dotted (solid) black line. Magnetic field lines are drawn as solid black lines; field aligned currents flowing along them are colored blue for downward, red for upward. These connect with lobe reconnection cells drawn in the dayside high latitude ionosphere. The vertical component of the terrestrial magnetic field in the equatorial plane is labeled B and illustrated in purple, the sudden commencement driven enhancement is b. Incoming solar wind with speed v_{SW} is indicated with orange arrows. The magnetopause current, J_{MP}, is illustrated with a green arrow. J_{MP} connects with a current (J_C, green) flowing across the compressional wavefront which is indicated with a dashed line (and moves according to the orange dashed arrow labeled V_C). (b) Time line of presented observations with respect to +SI onset in SYM-H at 20:19 UT on 16 June 2012.

Araki (1994) proposed a model for the propagation of SC effects through the terrestrial magnetosphere. They described the propagation in two modes: a compressional wave through the equatorial plane, and Alfvén waves along magnetic field lines to high latitude regions. An updated version of their Figure 12d is presented in Figure 1a, to help describe SC propagation. They proposed that when a pressure pulse compresses the dayside magnetosphere, the magnetopause moves inwards (shifting from the dotted line position Earthwards to the solid line magnetopause in Figure 1a). As a result, the magnetopause current (J_{MP} in Figure 1a) increases. This increased J_{MP} propagates tailward along the magnetopause, and at a given moment connects to J_C along the compressional wavefront (dashed green line in Figure 1a) for current continuity. J_C connects with J_{MP} to form a current loop. Due to the enhanced current within this loop, the vertical component of the Earth's magnetic field increases (by a factor b in Figure 1a); this results in a well observed rapid positive increase in SYM-H (e.g., Hori et al., 2015; Takeuchi et al., 2002).

Simultaneous to compressional propagation, Alfvén waves accompanied by field aligned currents (FACs) travel down magnetic field lines to their roots in the ionosphere. In the dayside northern hemisphere (NH) ionosphere, downward cusp FACs are observed on the afternoon side, and upward cusp FACs on the morning side. Corresponding tightly wound twin ionospheric convection vortices are observed in the NH dayside ionosphere, often noted as a signature of lobe reconnection (Chisham et al., 2004; Crooker, 1992; Imber et al., 2006) and observed under northward interplanetary magnetic field (IMF). These cells are clockwise in the afternoon sector, and anti-clockwise in the morning, and are connected with cusp auroral emission (e.g., Carter et al., 2020; Milan et al., 2022). Finally Araki (1994) predicted that SC effects would be rapidly countered by an opposing set of ionospheric currents, meaning the described set of FACs, convection vortices and cusp aurora would be rapidly extinguished. However more recent research suggests that SC effects continue until the compression ends (e.g.,

Gillies et al., 2012). It is important to note that Araki's model for SC effects has no dependency on IMF B_Z orientation, but the predicted signatures relating to lobe reconnection have since been shown to be related to northward IMF (Chisham et al., 2004; Crooker, 1992; Imber et al., 2006).

Magnetometer signatures will show a superposition of the signatures of these two propagation modes, depending on the latitude of the station. The compressional mode signature is a step change, which for a +SI (−SI) gives a sharp increase (decrease) in the vertical component of the Earth's magnetic field. The Alfvén mode results in a bipolar signature, the polarity of which depends on the position of the station in local time and latitude (e.g., Takeuchi et al., 2002). The relative timings of the arrivals of the compressional and Alfvén components of SI propagation at the ground has yet to be determined. There is some suggestion by Araki (1994) that the observed propagation signatures in magnetometer data are simultaneously superposed, suggesting the same arrival time for both modes. However, Araki (1994) also suggests that the Alfvén mode propagation starts after the compressional mode has passed the Earth and moved downtail; this suggestion is confirmed by modeling results from Fujita et al. (2003) and observations by Araki et al. (1997). Takeuchi et al. (2002) showed that the polarisation of Alfvén wave signatures in magnetometer data are consistent for positive and negative SCs, and showed a local time and latitude dependence of the direction of the preliminary impulse of the Alfvén signature. Additional to the described waveforms, Smith et al. (2021) showed large rates of change of horizontal component of magnetometer observations, and noted consequences for geomagnetically induced currents.

Solar wind pressure pulses vary greatly in magnitude, but even for a small pressure pulse, the effects of the resulting +SI on the high latitude ionosphere can be dramatic. The impact of an SI on the magnetosphere has been shown to result in a sudden increase in the amount of backscattered echoes received by SuperDARN radars (Coco et al., 2005, 2011; Gillies et al., 2012), regardless of the direction of the pressure change. Coco et al. (2011) attributes this increase in scatter to either soft particle precipitation in the F region as a result of field line resonance caused by Alfvén wave propagation, or increased precipitation of trapped magnetospheric particles due to the loss cone instability. Either way, such particle precipitation increases the ionospheric electron and ion densities and can seed F region irregularities, affecting SuperDARN backscatter returns. Positive SIs can result in enhancements in the twin cell flow, particularly the strength of antisunwards flow in the noon sector (Gillies et al., 2012; Hori et al., 2015). Conversely, Hori et al. (2015) showed that a −SI can induce reverse twin cell flow. There has also been some evidence of lobe reconnection type signatures in SuperDARN ionospheric convection maps, under B_Y dominant conditions (e.g., Coco et al., 2008). Additionally, in the superposed epoch analysis presented by Gillies et al. (2012), northward IMF drove SI intervals, whereas southward IMF drove SSC intervals.

Fujita et al. (2003) demonstrated polar latitude FAC generation following an SC using numerical simulation, while Kikuchi et al. (2001) investigated the differences between ionospheric and FAC effects. Similarly, Ozturk et al. (2017) showed convection vortices with associated FAC signatures as a result of rapid magnetopause compression through magnetohydrodynamic (MHD) modeling, with little change under different IMF B_Y orientations. Famously, Tamao (1964) predicted that a wave will take a certain path depending on whichever field line it couples to—this is known as the Tamao (1964) path. Chi et al. (2001) investigated the timescales of SC propagation through the magnetosphere, while Chi et al. (2006) showed that SC effects are propagated through Tamao (1964) paths using numerical simulations in a three dimensional magnetosphere. Finally, Boudouridis et al. (2003) showed significant changes in the size and intensity of the auroral oval as a result of an SC, particularly an increase in the latitudinal width of the auroral zone, but did not note any high latitude cusp emission.

In this paper, novel observations of the effects of a pressure pulse driven +SI on the terrestrial ionosphere will be presented, and examined in the context of propagation models. These are the first simultaneous observations of convection vortices, FACs, auroral emission, and magnetometer wave observations following pressure pulse compression resulting in +SI onset. First, the data products used across the observations will be described in Section 2. Then, the observations across solar wind, IMF and geomagnetic indices will be presented in Section 3.1, followed by ultra-low frequency (ULF) wave observations, high-latitude ionospheric convection, FACs and auroral images in Section 3. Finally, these observations will be consolidated to connect with models for pressure pulse/+SI effect propagation, followed by a discussion of results in Section 4 and concluding remarks in Section 5.

2. Data

In order to characterize the pressure pulse, 15 s resolution IMF (components B_X, B_Y and B_Z) are retrieved from the Magnetic Field Investigation instrument (Lepping et al., 1995) onboard the Wind satellite (e.g., Wilson

III et al., 2021) via NASA's CDAWeb (https://cdaweb.gsfc.nasa.gov/istp_public/). Also from the Wind satellite, despiked and merged plasma data from the Wind 3DP data set (Lin et al., 1995; Ogilvie et al., 1995; Von Rosenvinge et al., 1995) are retrieved from NASA's CDAWeb (https://cdaweb.gsfc.nasa.gov/istp_public/), specifically solar wind density and velocity. Wind data are propagated to the magnetopause using a method from Lester et al. (1993), which is discussed in detail in the next section. Further solar wind density, velocity and pressure data are retrieved from the OMNI archive (King & Papitashvili, 2005), which are propagated to the bow shock nose (Weimer et al., 2002, 2003; Weimer & King, 2008). OMNI data and documentation are available from OMNIWeb (https://omniweb.gsfc.nasa.gov/hw.html). Additionally, the auroral indices, AU and AL (Davis & Sugiura, 1966; World Data Center for Geomagnetism Kyoto et al., 2015), and SYM-H (Iyemori, 1990) are provided by the WDC for Geomagnetism, Kyoto (http://wdc.kugi.kyoto-u.ac.jp/wdc/Sec3.html) via the OMNI data set, and help to characterize the propagation of SIs into the terrestrial magnetosphere. AU and AL are the upper and lower envelopes respectively of the H component of magnetometer observations from 12 high latitude (most above 60°) magnetometers, which are distributed roughly evenly in longitude. SYM-H is the average deviation in the H component over 11 mid latitude magnetometers, and is analogous to the storm index Dst, but at minute resolution.

To probe the propagation mechanism of the SI, magnetometer observations of ULF waves are presented. The Canadian Array for Realtime InvestigationS of Magnetic Activity (CARISMA, Mann et al., 2008) is a network of ground-based magnetometers with stations across North America and is used here to characterize the dayside magnetospheric response. CARISMA magnetometers measure the three components of the Earth's magnetic field sensing fluctuations at ground level, and the network covers over 25° in magnetic latitude and 5 hr in magnetic local time (MLT) (Mann et al., 2008). CARISMA data is presented in X, Y, Z components, with the mean background subtracted and obtained via: http://www.carisma.ca/. SuperMAG (Gjerloev, 2012) is an international collaborative network of over 300 magnetometers, data from which used to analyze ULF wave effects here. SuperMAG data are provided in N, E, and Z components, with background presubstracted, and are obtained from stations across North America for this study via: https://supermag.jhuapl.edu/.

The Super Dual Auroral Radar Network (SuperDARN, Chisham et al., 2007; Greenwald et al., 1995; Lester, 2008, 2013; Nishitani et al., 2019) is an international consortium which builds and maintains high frequency radars across an expanding network of over 35 sites. Near global coverage is achieved in the polar regions. The network was conceived to study ionospheric convection: the horizontal circulation of the F region ionosphere, primarily driven by Dungey (1961) cycle effects. In this study, ionospheric convection maps are assimilated from SuperDARN data (obtained via the British Antarctic Survey Data mirror: https://www.bas.ac.uk/project/superdarn) using the map potential technique (Ruohoniemi & Baker, 1998) across all available NH radars, which generates excellent coverage over the dayside region. These convection maps are one of the key diagnostic tools used to probe the state of ionospheric electrodynamics, and are generated at 2 min resolution.

Additionally, field-aligned currents (FACs) rooted in the E region ionosphere are characterized using the Active Magnetosphere and Planetary Electrodynamics Response Experiment (AMPERE, B. J. Anderson et al., 2000, 2014; B. Anderson et al., 2002; Coxon et al., 2018; C. L. Waters et al., 2001; C. Waters et al., 2020). AMPERE is a data set which describes the FACs in both hemispheres using Iridium satellite data and is generated from engineering magnetometers onboard 66 telecommunications satellites, provided at 2 min resolution. The AMPERE data set is continuous, and provides measurements of both upward and downward FACs on a magnetic latitude—MLT grid. AMPERE data are available online via: http://ampere.jhuapl.edu.

Auroral images from the Defense Meteorological Satellite Program Special Sensor Ultraviolet (UV) Spectrographic Imager (DMSP SSUSI, Paxton et al., 1992) are used to characterize auroral emission and obtained from: http://ssusi.jhuapl.edu. The DMSP spacecraft are in polar, sun-synchronous orbits, and image both hemispheres about once every 1.5 hr (e.g., Carter et al., 2018). An entire scan of either hemisphere is built up over about 20 min of observations along the orbital path. SSUSI instruments are sensitive to UV wavelengths, separated into 5 spectral bands (e.g., Carter et al., 2018). The Lyman-Birge-Hopfield long (LBHl) band and Lyman-α bands (165–180 and 121.6 nm respectively) are used to characterize auroral emission associated with the +SI effects. These bands were selected as they are primarily driven by electron (LBHl) and ion (Lyman-α) precipitation. Finally, electron and ion spectrograms from the DMSP Special Sensor J (SSJ, Redmon et al., 2017) instrument are presented to allow an examination of particle precipitation over the auroral observations. This instrument measures the differential energy flux of particles with energies from 30 eV up to 30 keV.

3. Observations

In this section we use the datasets described in Section 2 to study a +SI event at 20:19 UT on 16 June 2012 as detected using the SYM-H index. In the following subsections observations of this event will be presented across solar wind and IMF parameters (Section 3.1); ULF wave observations in ground magnetometer data (Section 3.2); and coherent ionospheric signatures across ionospheric convection, FACs (Section 3.3), and auroral emission (Section 3.4).

3.1. Solar Wind, IMF, and Geomagnetic Indices

In this section the signatures of the observed pressure pulse and resulting +SI will be described in solar wind and IMF parameters, as well as geomagnetic indices. First, solar wind, IMF and geomagnetic indices will be presented in Figure 2 as a function of time (in minutes) relative to the onset of the +SI. Figure 2a shows the Y and Z components of the IMF, followed by the IMF clock angle in Figure 2b. Figure 2c shows the auroral indices AU and AL. Figures 2d and 2e shows the solar wind dynamic pressure, flow speed and particle density from OMNI and Wind respectively. Figure 2f shows the ring current index SYM-H, and Figure 2g shows the magnetopause stand off distance according to Shue et al. (1998).

In Figure 2, a combination of OMNI (Figure 2d) and Wind (Figures 2a and 2e) satellite data are presented (the contributing data set is labeled on the right hand side of the panel). SYM-H shows a rapid increase of magnitude around 30 nT over about 3 min, as presented in Figure 2f. From here on, the start of this signature at 20:19 UT on 16 June 2012 will be described as +SI onset for this event. SYM-H is fairly steady before +SI onset, and although there is some wave-type activity afterward (likely modulation of the H component as a result of ULF waves), the average magnitude is roughly steady. The overall signature is approximately a step-like change in field magnitude, which remains elevated afterward, consistent with the propagation of pressure pulse affects into the magnetosphere. AU (black) and AL (purple) are presented in Figure 2c; no substorm signatures are observed in this interval. There is a short lived spike in AU around +SI onset, but since it is characterized by only one data point no significant conclusions can be drawn on its relationship with +SI onset.

The solar wind particle velocity, V_{SW} (gold), particle density, N_{SW} (blue), and pressure P_{SW} (black) as retrieved from the OMNI data set are presented in Figure 2d. Just before and after the SYM-H +SI onset there are significant gaps in the timeseries, as well as elsewhere. There is also variability in the values after SI onset. Despite this, some general points can be made about the shape of the pressure curve. Before about 8 min prior to +SI onset, the pressure is fairly steady around 5 nPa; there is a subsequent OMNI data gap which lasts 6 min. 2 min before +SI onset in SYM-H, the pressure is around 13 nPa, double pre-onset values and significantly elevated above average values of a few nPa (e.g., Fogg et al., 2022). The pressure remains elevated above previous values, although there is variability in the timeseries and another data gap following the pressure increase. Hence the exact arrival time of the pressure pulse at the bow shock in P_{SW} cannot be determined, but may lie somewhere between eight and 2 min before the +SI onset in SYM-H. A similar argument can be made about N_{SW} and V_{SW} since they follow a similar shape to P_{SW}.

It is possible that the rapidity of a pressure pulse feature could result in unphysical features after the application of the OMNI propagation algorithm, due to the point by point propagation time calculation (Weimer et al., 2002, 2003; Weimer & King, 2008). Subsequently, such discontinuities will be removed, meaning rapid variations are not always captured well by OMNI. In this period, OMNI observations have been generated from data taken aboard the Wind satellite, so this source data was retrieved and propagated to the magnetopause using a single spacecraft method presented by Lester et al. (1993).

Before discussing the Wind observations, the propagation method for these observations will be briefly outlined. The Lester et al. (1993) propagation method relies on the assumption that the velocity of the phase front is constant, and the phase front is linear over a greater scale size than both the Earth-spacecraft distance along the Sun-Earth line and the scale size of the magnetosphere. The propagation time applied to the Wind data is defined in terms of the geometry of the spacecraft relative to the Earth, factors defining the time taken to traverse the magnetosheath (in Lester et al. (1993)'s notation $\beta = 0.25$), a field compression factor (in Lester et al. (1993)'s notation $\alpha = 3.0$), and the speed of the fast flow defining the pressure pulse that generates +SI onset. For full details of the propagation method, the reader is directed to Lester et al. (1993).

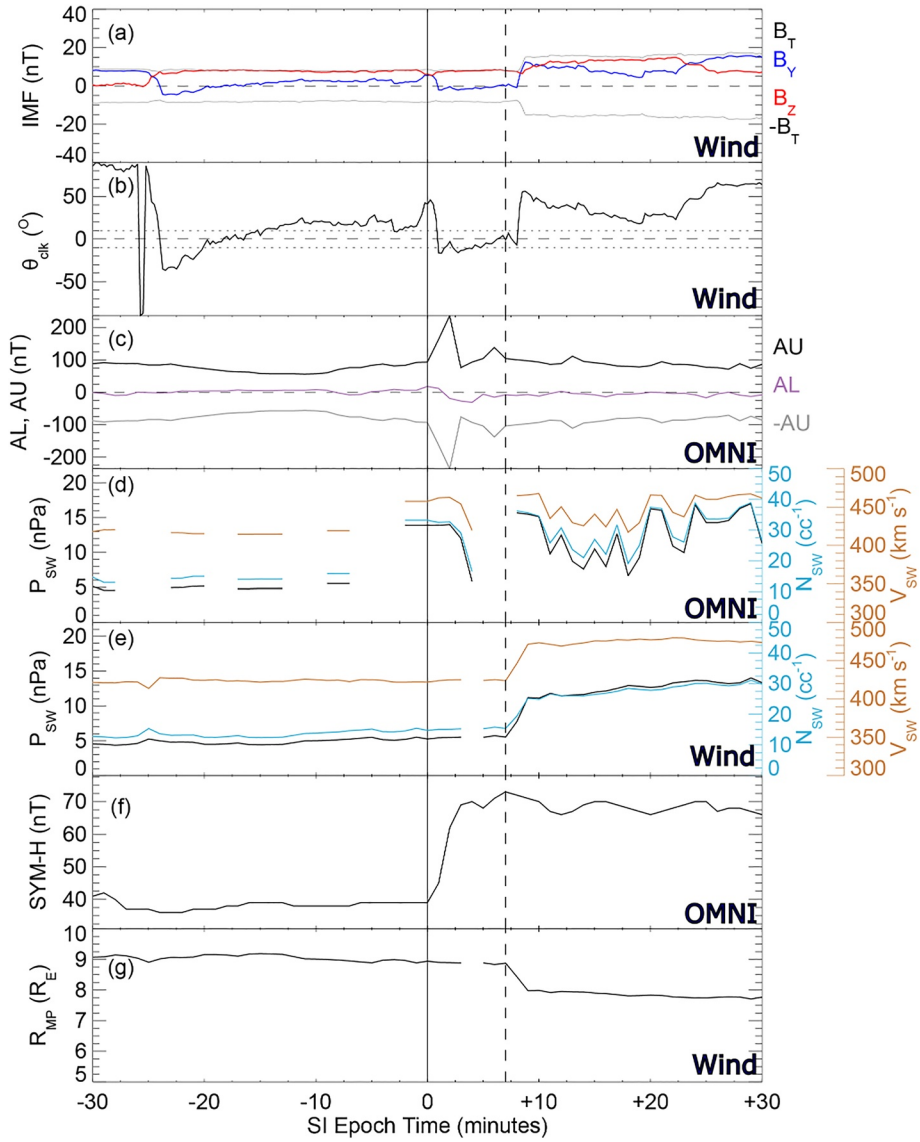

Figure 2. Timeseries of interplanetary magnetic field (IMF), solar wind and geomagnetic parameters relative to SYM-H +SI onset time at 20:19 UT on 16 June 2012 (solid vertical line). Parameters shown are (a) IMF B_Y (blue), B_Z (red) and $B_T = \sqrt{B_X^2 + B_Y^2 + B_Z^2}$ (gray) geocentric solar ecliptic from Wind MAG (b) IMF clock angle $\theta_{clk} = \tan^{-1}\left(\frac{B_Y}{B_X}\right)$ calculated from Wind MAG IMF (c) upper (AU, black) and lower (AL, purple) auroral electrojet indices (-1 * AU in gray) retrieved from OMNI (d) OMNI solar wind dynamic pressure (P_{SW}, black), flow speed (V_{SW}, gold), and density (N_{SW}, turquoise) (e) same as for (d) but from the Wind 3DP data set (f) ring current index SYM-H retrieved from OMNI (g) Shue et al. (1998) magnetopause stand off distance calculated from Wind data. All OMNI data is propagated to the bow shock, and Wind data has been propagated as described by Lester et al. (1993).

Solar wind density N_{SW} (blue) and velocity V_{SW} (gold, x component is presented as it is dominant in this interval) from the Wind 3DP data set are presented in Figure 2e, with the solar wind dynamic pressure $P_{SW}\left(\approx N_{SW}V_{SW}^2\right)$ in black. A clear pressure pulse signature is observed in this interval, with its onset indicated with a dashed vertical line. This signature appears both after the possible onset in OMNI data (+SI onset -8 to -2 min), and the onset as detected in SYM-H.

It would not be physical for the pressure pulse signature to arrive at the magnetopause after both the signatures in OMNI P_{SW}, SYM-H, and magnetometer signatures presented later. Hence there must be some inaccuracies associated with the calculated propagation time, which may come from multiple sources. Firstly, the assumption that the pressure pulse phase front is linear may not be correct, although multiple satellites are not available to

test this assumption. Secondly, there may be a flaw in the propagation method itself, likely to do with the single spacecraft calculation of the angle of the phase front. To overcome these issues, complete observations of the shape and direction of travel of the pressure pulse could be determined from multiple upstream spacecrafts, if they were available. Nevertheless, it is likely that this event is associated with the SYM-H signature since the pressure pulse is a clear signature amongst otherwise steady P_{SW}.

High resolution IMF B_Y and B_Z observations from Wind are propagated as for the plasma measurements, and presented in Figure 2a in blue and red respectively. The calculated total magnetic field, $B_T\left(=\sqrt{B_X^2+B_Y^2+B_Z^2}\right)$ is also presented in gray. B_Z is steadily positive throughout the interval, except a small excursion around zero at the beginning. The magnitude of B_Y is always lower than B_Z, except short excursions at the beginning and end, and just following the pressure pulse arrival (the arrival time for Wind data is indicated with a dashed line). At the pressure pulse arrival time, there is a small increase in B_Z, and a rapid increase in B_Y, which together cause a small magnitude rapid increase in B_T. This causes a rapid change in the clock angle ($\theta_{clk}=\tan^{-1}\left(\frac{B_Y}{B_Z}\right)$ and presented in Figure 2b), despite the low magnitude of the changes. Therefore any IMF effects during the presented period are dominated by the B_Z component, apart from the initial period around onset where an increase in B_Y dominates the clock angle. It is important to note that a strong B_Y under northward IMF conditions has been shown to increase the dayside reconnection rate (e.g., Grocott et al., 2003, 2004, 2008). So although the B_Y change is of small magnitude, some enhancement of dayside driving may be expected as a result.

Finally, the magnetopause stand off distance, R_{MP}, which is calculated using the model equatorial magnetopause presented by Shue et al. (1997), (1998), is presented in Figure 2g, and calculated using the propagated Wind plasma and IMF data. R_{MP} decreases rapidly by about 1 Earth radii (R_E, almost 10%) at the Wind pressure pulse arrival time. This magnetopause compression is sustained as long as the solar wind dynamic pressure remains elevated. Overall, the observed pressure pulse and the related +SI are clear and distinct, and there are no other obvious external phenomena driving the solar wind-magnetosphere-ionosphere interaction in this period apart from a small IMF rotation, which may lead to increased driving as a result of IMF B_Y.

3.2. ULF Wave Propagation

Observations from a chain of CARISMA (Mann et al., 2008) magnetometers stationed closest to noon MLT at the onset of the SI in SYM-H are presented in Figure 3. The chain is made up of four stations, whose individual traces are presented in different panels, labeled with station identifier, geomagnetic latitude, and their local time at +SI onset. The stations cover eight degrees in latitude along roughly the same local time position. They are presented in X, Y, and Z coordinates, which point north, east and vertically down respectively, and are colored green, purple, and pink in Figure 3.

First, the effect of the SI on the geomagnetic north/south component of the magnetometer signal, B_X, will be examined. Each station records a bipolar signature in B_X, although the magnitude of this is clearest for higher latitude stations FCHP and MCMU. This is followed by wave-like oscillations in magnitude, which are centered on a line of higher magnitude than the preceding period. Together, the observations show a superposition of the bipolar Alfvén and step change-like compressional components of the SI propagation. The wave-like oscillations that follow are of highest magnitude at the lowest latitude station, GULL. This may be evidence of field line resonance (Southwood, 1974) excited by the impact of the pressure pulse at the dayside magnetopause. It is important to note that the Alfvén wave component is rotated as it passes through the ionosphere (Hughes & Southwood, 1976), whereas the compressional component is not (Kivelson & Southwood, 1988; Yeoman et al., 1990). Similar signatures are seen in the eastward, B_Y component, which is presented in purple; the GULL station shows decreasing magnitude oscillations. Although the magnitude of the variations in the vertically down component, B_Z, are much smaller, some bipolar signatures are seen, with oscillations most uniform at the GULL station.

To summarize, observations from the chain of CARISMA magnetometers closest to noon have been examined, and clear +SI signatures are observed. The SI propagates through the magnetosphere in two modes: evidence of Alfvén mode propagation is observed, and the compressional mode is observed to propagate more efficiently to lower latitude. Additionally, there is some evidence that due to Tamao (1964) path effects higher latitudes are communicated the effects of the SI first, particularly with the B_Z component which shows +SI effects later with decreasing latitude. However +SI onset is seen almost simultaneously in the other components. These

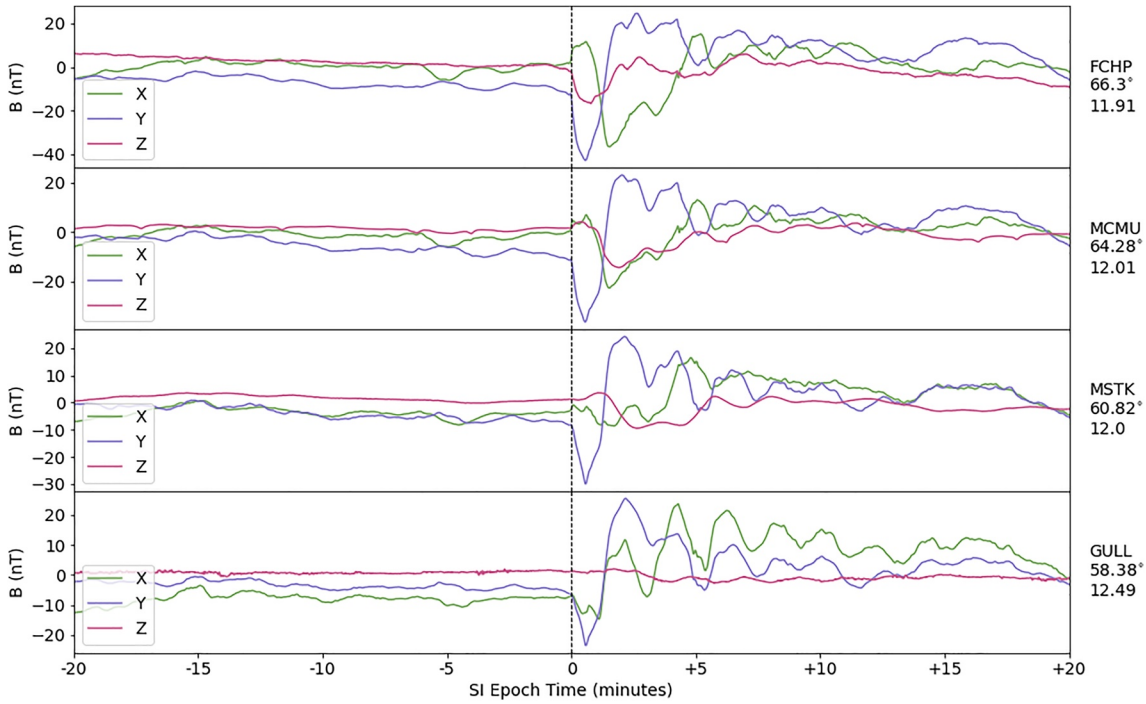

Figure 3. Timeseries of magnetometer observations from the CARISMA data set with respect to +sudden impulse (SI) onset at 20:19 UT on 16 June 2012. Each panel shows a different station, labeled on the right with its geomagnetic latitude and local time at +SI onset. Data are presented in *X*, *Y*, and *Z* components in green, purple, and pink respectively.

possible differences were observed over a relatively small latitude range, so more pronounced differences would be expected in equatorial and polar observations.

To investigate these latitude differences, a chain of SuperMAG magnetometers were extracted, with a larger range in latitude; this is presented in Figure 4. SuperMAG data is presented in *N* (magnetic north, left column), *E* (magnetic east, center column), and *Z* (vertically down, right column) components, with individual stations labeled on the right hand side of each panel with their geomagnetic latitude and local time at +SI onset. Focusing on the *N* component, a primarily Alfvén type signature is seen at high latitudes (≈70°), with some decaying oscillations that follow. At around 58–60°, a superposition of both Alfvén type bipolar signatures and compressional type step change is seen in the data. By about 40°, a primarily compressional type step increase in the magnitude is observed. The *E* component is similar across all latitudes, but the *Z* component shows oscillations stratified by latitude, although less clearly than in N. This evidence reinforces the Araki (1994) model, showing that at +SI effects are communicated more efficiently by Alfvén modes at higher latitudes, and compressional modes at lower latitudes.

These results were compared with simulation outputs using the numerical MHD model of Wright and Elsden (2020). This linear model is effective at studying MHD wave propagation in a background dipole magnetic field, in high spatial and temporal resolution. Another important feature of this model is the ability to apply a boundary condition directly at the magnetopause, which allows for the input of a step-like jump in the pressure to model the pressure pulse which drives the +SI. This differs from many global MHD models, where the upstream boundary conditions have to be specified much further from the Earth (e.g., 30 R_E upstream (e.g., Claudepierre et al., 2010; Oliveira & Raeder, 2014)). The analysis of these simulations is ongoing, though initial results show favorable agreement with the observations presented here. However, these will be fully presented and discussed in a follow-up modeling study and therefore further discussion is beyond the scope of the present paper.

Finally, there is some evidence of a small temporal lag in the receipt of SI effects based on SuperMAG magnetometer latitude—confirming observations from CARISMA data. Focusing on the *N* component, in Figures 4a–4o, some lower latitude station signatures begin later than higher latitude stations, for example, T25 station at 51.05° in Figure 4n.

10.1029/2022JA031136

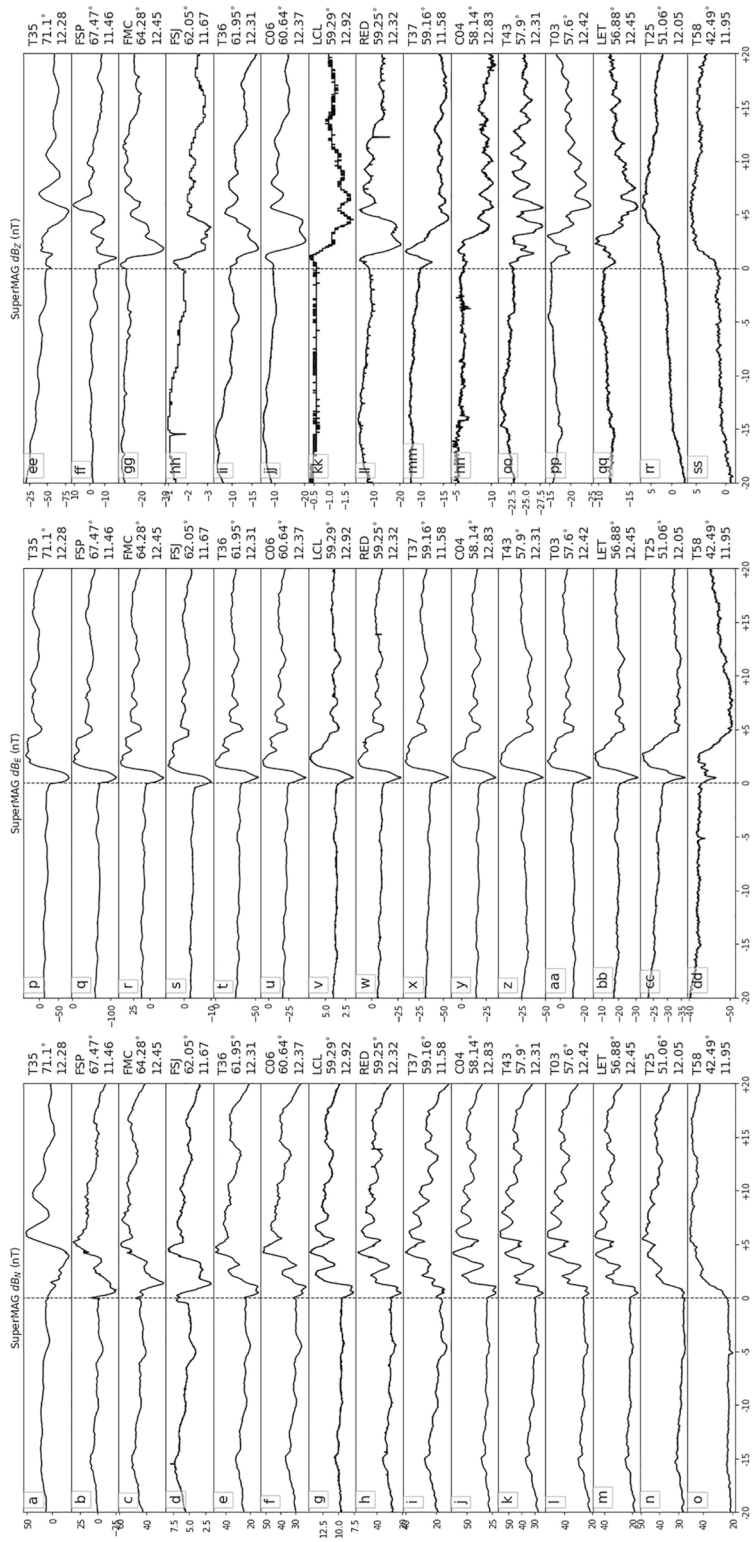

Figure 4. Timeseries of magnetometer observations from the SuperMAG data set with respect to +sudden impulse (SI) onset at 20:19 UT on 16 June 2012. Left column (a–o) shows component *N*, center column (p–dd) shows component *E*, and right column (ee–ss) shows component *Z*. Individual stations are labeled at the right of the panel with their geomagnetic latitude and local time at +SI onset. Stations are presented in descending latitude top to bottom. Note that stations C04 and C06 are the same as stations GULL and MSTK in Figure 3.

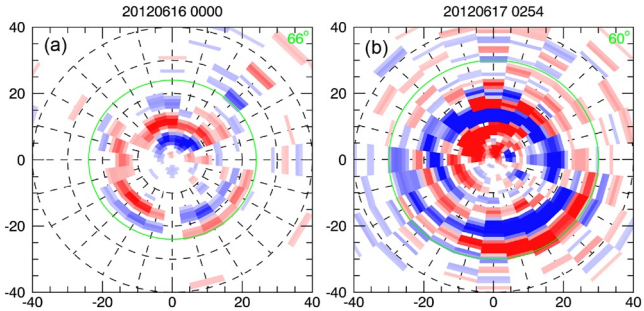

Figure 5. Magnetic latitude—magnetic local time maps of AMPERE field aligned current data from (a) 00:00–00:02 UT 16 June 2012 (b) 02:54–02:56 UT 17 June 2012. Noon is at the top, dawn on the right. Upward currents are colored red, downward in blue; increasing color strength equates to increasing current density. Axes are labeled in degrees colatitude. Manually fitted circles (green) are overplotted with the midnight meridian latitude recorded in the top right hand corner.

Magnetometer signatures of +SI propagation have indeed been presented before, for example, by Araki (1994) and Takeuchi et al. (2002), and these magnetometer observations confirm previous results. However, the observations in other datasets that follow are novel, and the inclusion of the magnetometer observations here helps to provide a full picture of +SI propagation effects, and enables comparison with previously presented events.

3.3. Ionospheric Convection and Field Aligned Currents

Ionospheric convection maps generated from SuperDARN data will be used to characterize F region ionospheric flows. These maps were created using the map potential technique (Ruohoniemi & Baker, 1998) from line-of-sight (LOS) velocity measurements recorded at radars across the NH. All available radar data from NH stations was processed using FitACF 3.0; a detailed discussion of the affect of FitACF 3.0 on convection maps is described in the appendix of Fogg (2021). Both traditional, and Fogg et al. (2020) style Heppner-Maynard boundary (HMB) latitude estimation resulted in rapid temporal jumps in latitude due to the dynamically evolving conditions, which were unrepresentative of the smoothly varying expanding and contracting polar cap, and so a different technique was used here.

The latitude position of the HMB was determined by manually fitting circles to AMPERE FAC maps at 2 min resolution; this is permissible as it was shown by Fogg et al. (2020) that there is a linear relationship between the size of the AMPERE FAC region and the SuperDARN convection region as a result of the expanding and contracting polar cap paradigm (Cowley & Lockwood, 1992; Lockwood & Cowley, 1992; Milan, 2013; Milan et al., 2003, 2007). A green circle centered on the geomagnetic pole is plotted over a FAC map, and the latitude radius is manually adjusted so that it encompasses the FAC region, as presented in Figure 5. The latitude where the circle intersects the midnight meridian is recorded, and used to predict the entire HMB as a function of MLT in the map potential technique. Two examples of this manual fitting are presented in Figure 5 to demonstrate how the boundary position was chosen when the FAC pattern did not conform to the canonical Region 1/Region 2 (R1/R2) pattern (Iijima & Potemra, 1976a, 1976b).

The response of dayside ionospheric convection only is plotted in Figure 6, for brevity but also since the key effects are expected to be (and indeed are) observed in the dayside region. The region between 6 and 18 MLT, and 70° and 90° latitude is presented in the left hand column of Figures 6a–6s, with SuperDARN ionospheric convection data overplotted on top of coastlines. Each dot represents an observation, with color and flagpole length indicating the strength of flow; flagpoles point in the direction of flow. The convection streamlines, also equipotential contours, are drawn in black. The +SI onset occurs in Figure 6j, in the integration period 20:18-20:20 UT.

Before +SI onset, the convection pattern is roughly a twin cell configuration, and is constrained by significant patches of scatter on the dayside (Figure 6a). A signature resembling lobe reconnection (Crooker, 1992) appears at 20:08 UT in Figure 6g: vectors swirl clockwise around a circular electrostatic potential peak (×). Velocity magnitude is reduced compared with previous times—velocities must slow before they can change direction as the ionosphere is incompressible. By Figure 6j at 20:18 UT, the flows have strengthened and are circulating around a clear lobe cell on the dawn side. Although the vector observations are more sparse, there are also indications of a lobe cell on the dusk side. By 20:28 (Figure 6m), clear twin lobe reconnection cells are observed, which are well constrained by vector observations; velocities are strongest in the central sunwards flow. These signatures persist until 20:44 UT (not shown) when they start to decay away, and the circulation reconfigures.

Similarly, AMPERE FAC maps over the dayside only are presented in the middle column of Figure 6b–6t at 10 min intervals centered on +SI onset. An hour before onset, R1/R2 configuration is observed in the morning sector, as presented in Figure 6b, along with some upward current signatures which are not dominant features. By 20:08 UT (Figure 6h), around 10 min before +SI onset, clear R0 signatures are observed, roughly collocated with the beginnings of lobe reconnection cells in SuperDARN data (these are presented together in Figure 6i). These signatures begin as a result of continued northward IMF. As northward IMF persists, these signatures strengthen further by 20:18 UT (Figure 6k), and have become the dominant FAC feature around +SI onset. These R0 FACs

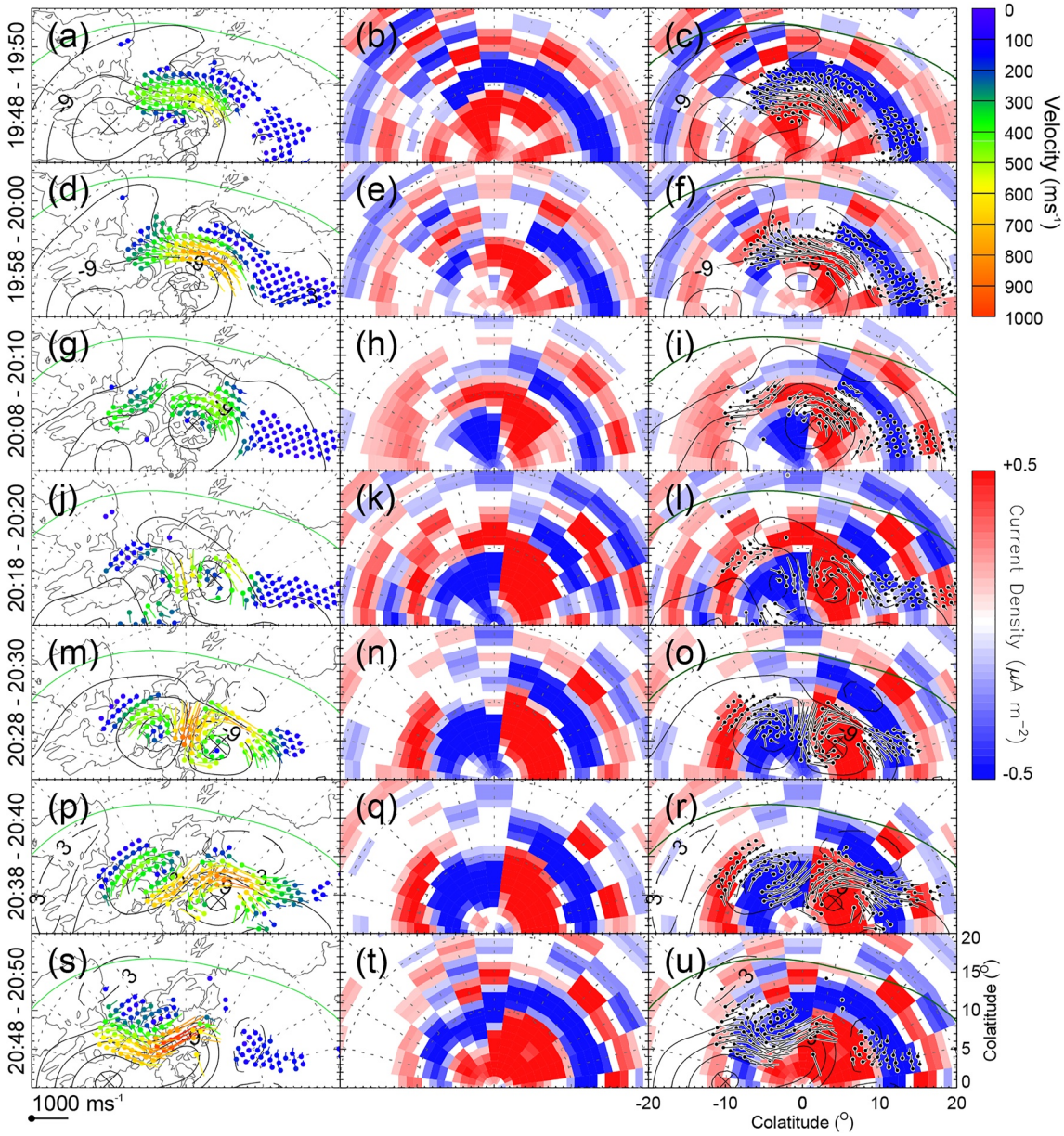

Figure 6. Magnetic latitude—magnetic local time (MLT) maps of (a–s) SuperDARN ionospheric convection maps, (b–t) AMPERE field aligned current (FAC) maps, (c–u) SuperDARN ionospheric convection maps overplotted onto AMPERE FAC maps. Each panel shows the 6–18 MLT sector with noon at the top, from 70° to 90° latitude. Each row shows an integration period 10 min later than the previous row, with the integration period recorded on the left hand side. Lines of equal latitude and MLT are plotted as dashed gray lines, and coastlines (left hand column only) are plotted as solid gray lines. Electrostatic equipotential contours/streamlines of flow are drawn in black, number indicates the potential. Velocity vectors are colored (left hand column only) to indicate the magnitude of the velocity according to the scale on the right, and flagpoles have length representing the speed as in the key in the bottom right. Flagpoles point in the direction of flow. The Heppner-Maynard boundary is drawn in green. AMPERE FAC densities are colored by their strength according to the scale on the right; upward currents are presented in red, downwards in blue.

persist and perhaps even strengthen by Figure 6q, before beginning to decay away. These Region 0 (R0) features are collocated with the SuperDARN lobe reconnection cell observations, and both datasets are presented together in the right hand column of Figure 6c–6u.

A timeseries of parameters relating both to the SuperDARN convection maps and AMPERE FAC maps discussed previously is presented in Figure 7, with +SI onset indicated as a vertical line. In Figure 7a, the cross polar cap potential (CPCP, Φ_{PC}, pink) and peak potentials (Φ_{max} and Φ_{min}, purple and blue) are presented. For Φ_{PC} and Φ_{min}, values start to weaken about 10 minutes before +SI onset, but begin rapidly increasing a few minutes before

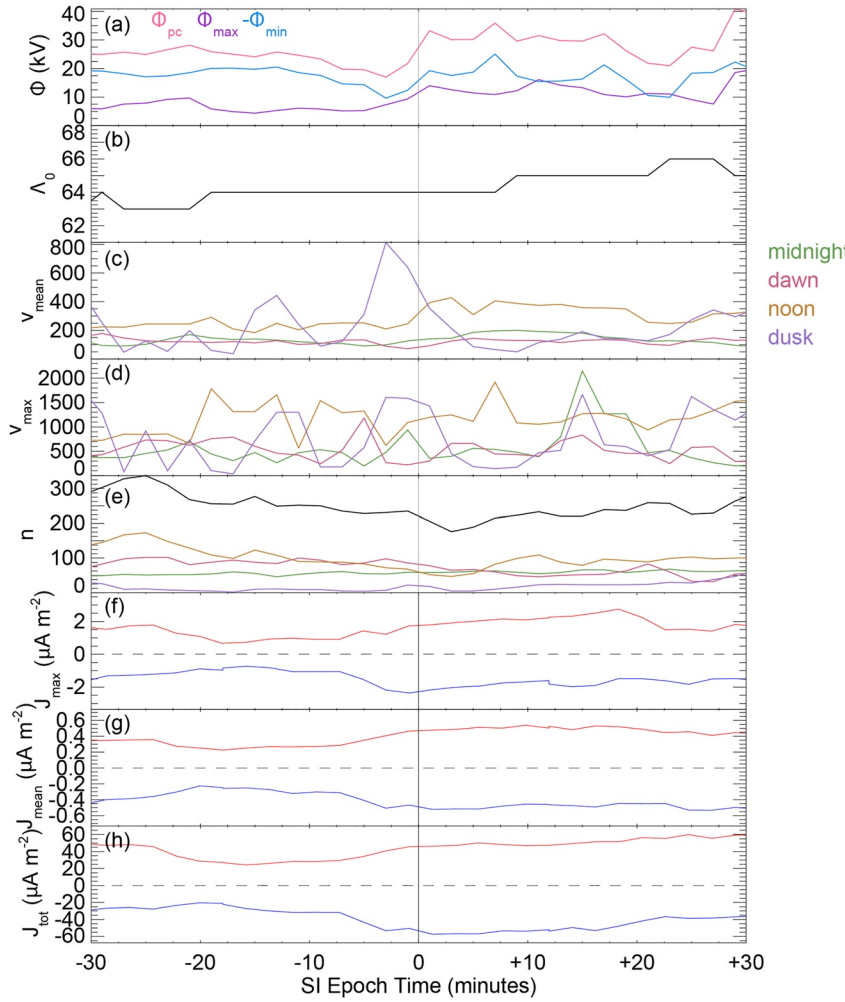

Figure 7. Timeseries of ionospheric parameters relative to SYM-H +sudden impulse onset time at 20:19 UT on 16 June 2012 (a) cross polar cap potential Φ_{PC} (pink, kV) and peak potentials Φ_{max} and Φ_{min} (purple and blue, kV) (b) the midnight meridian latitude of the manually positioned Heppner-Maynard boundary (Λ_0, °) (c) mean velocity (m s^{-1}) in four magnetic local time (MLT) sectors (d) maximum velocity (m s^{-1}) in four MLT sectors (e) number of vectors in four MLT sectors and overall (black) (f–h) maximum, mean and total AMPERE field aligned current current density; red for upwards currents, blue for downwards currents.

+SI onset. After +SI onset, Φ_{PC} is elevated around 10 kV above values at the start of the interval (about 15 kV above reduced values). This describes observations of slowing and then enhanced flows presented in Figure 6. Although Φ_{max} does not decrease beforehand, an enhancement is observed on a similar timescale to the other two parameters. The elevated values persist for around 20 min after the SI onset. This elevation in electrostatic potentials, in particular Φ_{PC}, is likely due to a combination of effects. First, it is evidence of the reconfiguration of ionospheric convection following the change to northward IMF—flows must slow (and hence Φ_{PC} decreases) before they can change direction, followed by an increase in flow speed and Φ_{PC}. Since the pressure pulse arrival is anywhere between 20:11 and 20:17 UT in OMNI, the uptick in Φ_{PC} is likely due to a combination of pressure pulse/SI enhancements and northward IMF. Although a B_Y rotation is also observed, no asymmetries are observed in the convection data, so it is argued here that the B_Y effects are not dominating the Φ_{PC} enhancements. Additionally, the midnight meridian latitude of the manually positioned HMB (Λ_0) is presented in Figure 7b. There is an increase in Λ_0 after the onset of the SI, but since this increase matches the resolution of Λ_0, it may not be physically significant.

In Figures 7c and 7d, the mean and maximum of the magnitude of LOS velocity vectors in four MLT sectors is presented. The sectors are defined as follows: 3 < MLT ≤ 9 (dawn, magenta), 9 < MLT ≤ 15 (noon, orange),

$15 < \text{MLT} \leq 21$ (dusk, purple), MLT > 21 and $MLT \leq 3$ (midnight, green); where colors indicate their depiction in Figures 7c–7e. For the v_{mean}, there is no noticeable change in midnight or dawn velocities. At noon, v_{mean} is enhanced by about 200 m s^{-1}, roughly double pre-onset values. This enhancement begins just before +SI onset, corresponding with Φ_{PC}. At dusk, the mean velocity is highly variable before the onset, but this variability is reduced after the onset. The maximum observed LOS velocity is presented in Figure 7d for the four MLT sectors. There is a great deal of variability in v_{max} across all MLT sectors, so it is difficult to see any clear changes related to +SI onset. At dusk, there is a slightly prolonged reduction in v_{max}, shortly following the SI, but it is indistinguishable from other changes due to high variability. Finally, the number of vector observations is presented in Figure 7e, in the four MLT sectors defined above, and at all local times (black). At midnight, dawn and dusk, the number of vectors is steady throughout the interval. At noon, the number of vectors decreases before +SI onset, and starts to increase about 5 min after +SI onset. This confirms the qualitative observations of changes in vector coverage. The shape of the curve for vectors at noon dominates the shape of the curve for vectors at all local times.

The maximum (J_{max}), mean (J_{mean}), and total (J_{tot}) AMPERE FAC current density between 6 and 18 MLT and 75°–90° latitude, and calculated from upward (red) and downward (blue) signatures are presented in Figures 7(f), 7(g), and 7(h) respectively. These parameters were calculated over a region roughly encircling the R0 currents presented in Figure 6, to quantitatively characterize the changes in current density around +SI onset. About 8 minutes before +SI onset in SYM-H, J_{max}, J_{mean} and J_{tot} begin to increase in magnitude for both upward and downward currents, and remain elevated long after +SI propagation begins. The only exception is that J_{max} for upward currents decreases slightly about 20 min after the SI onset.

From these observations, it appears at first that the enhancement in FAC density begins before the +SI is observed in SYM-H. However, the entire local time—latitude AMPERE coverage is resampled every 10 min, but each Iridium satellite takes measurements at 2 min resolution. Therefore 2 min resolution data contains some data taken ahead of the time it corresponds to. For example, at a 2 min resolution time interval, t, the FAC map contains data from t to $t + 10$. This will impact both the timing and the gradient of the observed enhancement. The enhancement appears to begin before the onset of the +SI as a result of the inclusion of measurements from after onset time, and the shape of the enhancement is smoothed somewhat.

3.4. Cusp Auroral Emission

Auroral observations from two UV wavelength bands from the DMSP SSUSI instrument are presented in Figure 8. Each panel shows a satellite pass, and is labeled at the top with the observing satellite, frequency band and start time of the pass (which is approximately 20 min (e.g., Carter et al., 2018)). At 19:53 UT, the F16 satellite begins a pass over the NH, prior to the pressure pulse arrival. In this pass, the auroral oval is clearly seen in LBHl (Figure 8a), with some similar signatures in Lyman-α (Figure 8b). There are no distinct polar cap emissions observed in either band at this time. The F18 satellite begins a pass across the NH at 20:20 UT, and in both wavelength bands the auroral oval can be identified, along with a small patch of emissions poleward of the auroral oval. This patch is slightly dawnwards of the pole (although it is close to the edge of the field-of-view), and is more bright in Lyman-α (Figure 8d) than in LBHl (Figure 8c). Since each pass lasts around 20 min, this patch is observed around 20:30 UT, and is hence roughly collocated with the dawnside clockwise lobe reconnection and upwards R0 currents. After +SI effects have decayed away in other datasets, at 21:33 UT, F16 begins a pass, in which the patch is no longer observed, although the auroral oval is brighter and wider. Later, there appears a long duration cusp spot, observed in detail by Carter et al. (2020).

There are two possible causes of cusp aurora collocated with R0 FACs under northward IMF (known as "NBZ" aurora). Either the upward FAC mechanism described by Carter et al. (2018) or magnetospheric precipitation associated with dayside reconnection, described by Milan et al. (2000); Frey et al. (2002). Observation of cusp auroral emission in the Lyman-α band suggest that the latter mechanism is present in this case, since the Carter et al. (2018) mechanism suggests only an electron signature would be present. It is important to note that due to the temporal resolution of the DMSP orbits, it is not possible to ascertain whether the cusp emission was caused or enhanced by pressure pulse arrival and the resulting SI onset, or whether it occurs simply as a result of northward IMF. However, since NBZ aurora and R0 FACs were shown to be correlated by Carter et al. (2018) it is likely that an auroral enhancement occurred corresponding to the enhancement of R0 currents. This potential enhancement could be driven by the enhancement of dayside reconnection following SI onset, a suggestion which is reinforced by the particle spectrograms presented next, or indeed possible particle precipitation relating to Alfvén wave propagation.

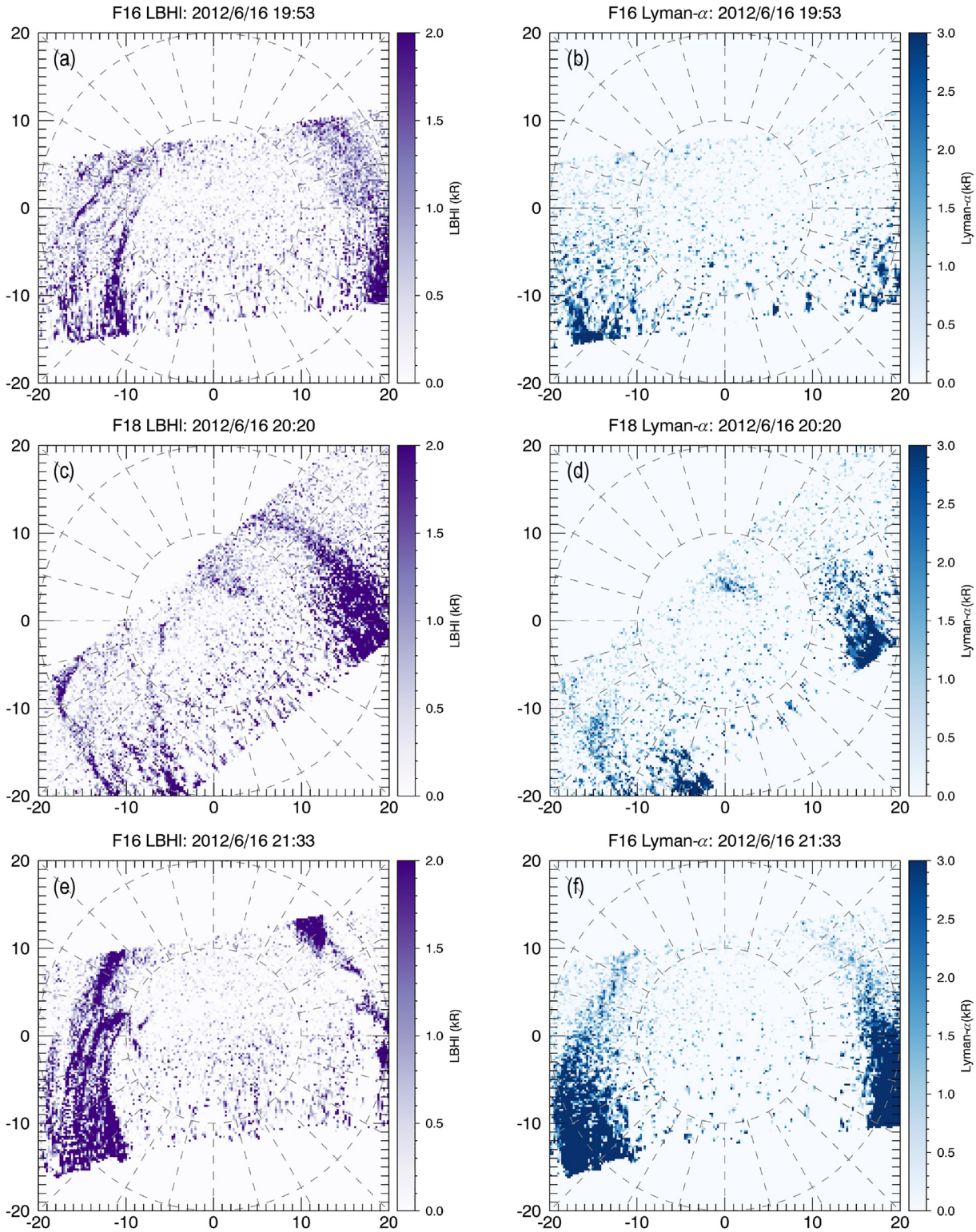

Figure 8. Magnetic latitude—magnetic local time maps of northern hemisphere Ultraviolet auroral observations from the DMSP SSUSI F16 and F18 satellites. Each panel is labeled at the top with the observing satellite, start UT of the pass and the wavelength band. LBHl emissions (left hand column) are between 165 and 180 nm, and Lyman-α emissions (right hand column) are at 121.6 nm.

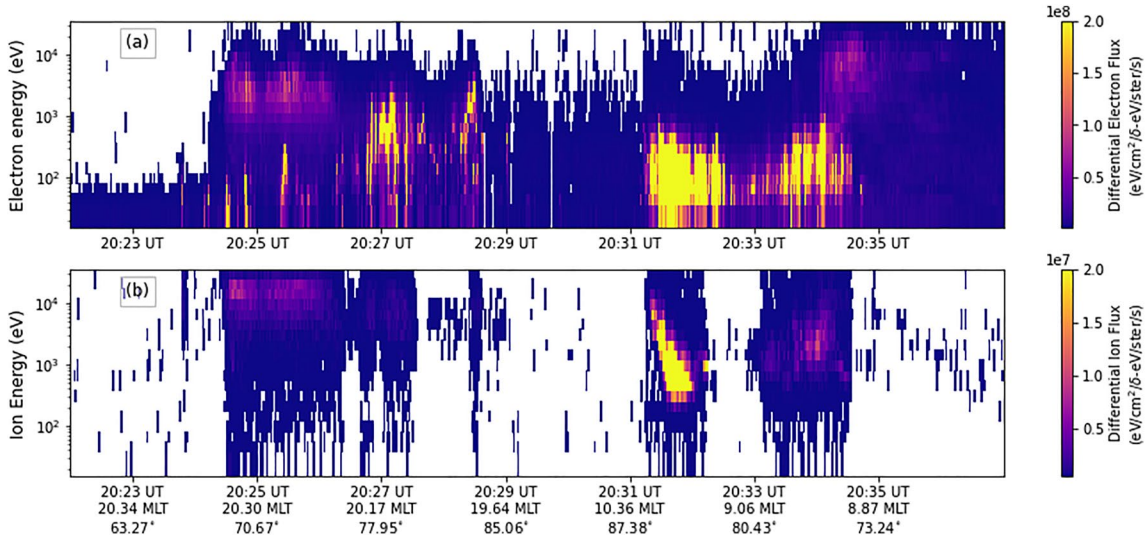

Figure 9. (a) Electron spectrogram (b) ion spectrogram. Both from DMSP Special Sensor J (satellite F18) on 16 June 2012. Xticks indicate the universal time (UT), spacecraft altitude-adjusted corrected geomagnetic coordinates magnetic local time and magnetic latitude.

In Figure 9, particle spectrograms from DMSP SSJ are presented from the F18 orbit shown in Figures 8c and 8d. It is important to note that the satellite is bisecting the track displayed in Figures 8c and 8d, moving from left to right in the panel. F18 passes over the observed cusp emission just after 20:31 UT, with signatures observed in both electrons and ions in Figures 9a and 9b. Precipitating electrons are observed across most of the electron energy bands in Figure 9(a), but high fluxes are observed at the lower end of electron energies. In the ion spectrogram (Figure 9b), an ion dispersion signature is observed. This is indicative of recent polar latitude lobe reconnection (Chisham et al., 2004, and references therein): as reconnection occurs, higher energy ions precipitate down magnetic field lines quickest, and are observed first. Lower energy ions precipitate down magnetic field lines more slowly, and hence are observed later. This clear indication of recent lobe reconnection is observed as the satellite passes over the cusp emission: confirming that the cusp emission is likely associated with the lobe reconnection signatures observed in SuperDARN convection maps (Figures 6a–6s). Additionally, these observations are also similar to spectrogram observations over the cusp spot observed by Carter et al. (2020).

4. Consolidated View of Observations

In this section, a final summary of all observations is given, drawing together the results from Section 3. A timeline of these observations is presented in Figure 1b. Some key observations are mentioned here in chronological order:

1. 20:08–20:10 UT: Lobe reconnection type signatures are observed in SuperDARN data, collocated with AMPERE R0 FACs. This is a result of the onset of northward IMF.
2. 20:11–20:17 UT: Pressure increase may occur in OMNI here.
3. 20:18–20:20 UT: CPCP, noon F region velocities and R0 FACs are elevated due to a combination of northward IMF and SI effects.
4. 20:19 UT: Superposition of ULF waves observed in magnetometers, stratified in morphology and arrival time by latitude.
5. ≈20:30 UT: Cusp emission observed in DMSP SSUSI collocated with lobe reconnection and R0 FACs.
6. ≈20:31 UT: Ion dispersion signatures from DMSP SSJ indicate recent lobe reconnection onset.

A key result in this study is the observation that the Alfvén wave component of +SI propagation dominates observations at high latitudes, and the compressional mode dominates at lower latitudes. This is seen in the latitudinal stratification of magnetometer traces which also show that the Alfvén component propagates to the high latitude regions slightly before the compressional component reaches the lower latitude regions. This evidence fits with the Araki (1994) model of SC propagation through the magnetosphere, and also demonstrates Tamao (1964) path effects on wave propagation.

The observation of clear lobe reconnection cells in SuperDARN data collocated with AMPERE R0 FACs preceding +SI onset matches with the northward IMF conditions, and is a novel observation combining these two datasets. Pressure pulse arrival and resulting +SI onset enhances these phenomena, demonstrating the effects of pressure pulse-driven compressions on the high latitude dayside ionosphere. It is important to note that there may also be some IMF B_Y effects in these observations, as there is a slight B_Y rotation simultaneous with the pressure pulse arrival; however since the B_Y magnitude is mostly below the B_Z magnitude, and no B_Y asymmetries are observed, it is likely that pressure pulse effects dominate. Additionally, and with some caveats based on limited temporal resolution, cusp auroral emission (from DMSP SSUSI) is observed following +SI onset, likely as a result of magnetospheric precipitation. This suggests that following +SI onset, particles precipitate down dayside magnetic field lines undergoing lobe reconnection, exciting auroral emissions. These particles may also trigger the generation of F-region ionospheric irregularities resulting in observed increases in SuperDARN backscatter. Although ion dispersion signatures also suggest the recent onset of lobe reconnection, it is possible that the cusp emission has lasted for the entire period of northward IMF, as interpretation is limited by DMSP SSUSI temporal resolution.

This is the first observation of the high latitude ionosphere around +SI onset simultaneously across the presented data sets. Additionally, these observations show the enhancement of the high latitude ionosphere as Araki (1994) suggested, with tightly wound lobe reconnection-type vortices and associated R0 FACs and auroral emission. However, unlike predictions by Araki (1994), but similar to more recent work by Gillies et al. (2012), these effects persisted for as long as the compression lasted. This work enhances our understanding of the effects of pressure pulse driven compressions by providing the chronology of +SI propagation across multiple datasets and phenomena for the first time. This demonstrates what sort of observations are needed to improve understanding of +SI phenomena: for example, a follow up statistical study using similar datasets to those presented in Fogg (2021). Indeed, this work also presents the first observation of lobe reconnection signatures in SuperDARN data under primarily northward IMF and enhanced by SI effects, with good vector coverage defining the convection cells.

5. Conclusion

An exciting and most novel observation in this paper, is the existence of lobe reconnection cells collocated with R0 FACs, both of which are enhanced by SI onset. With limited interpretation due to temporal resolution of the data, DMSP SSUSI images show cusp emission following SI onset, with corresponding particle precipitation signatures indicative of lobe reconnection. This agrees with the Araki (1994) model, which suggests lobe reconnection type signatures would occur at onset—and hence enhance the pre-onset pattern observed. However, Araki (1994) suggests that they would quickly be dissipated by a counter system, which is not observed here.

The observations of ULF wave modes at SI onset also agree with the Araki (1994) model, and show clearly over a wide range in latitude that Alfvén waves are dominant at higher latitudes, and the compressional mode dominates propagation at lower latitudes (although all latitudes showed a superposition of both modes). Additionally, magnetometer traces show that the higher latitude regions feel the effects of +SI propagation before the lower latitude regions. This suggests that Alfvén mode waves reach the high latitude ionosphere faster than compressional waves reach the low latitude ionosphere. Although similar ULF wave observations have been presented before, the observations presented here aid understanding of the chronology of +SI effect propagation, and enable easier comparisons with previously published events.

Data Availability Statement

Wind IMF and plasma data were retrieved from NASA's CDAWeb https://cdaweb.gsfc.nasa.gov/istp_public/. We gratefully acknowledge use of NASA/Goddard Space Flight Center's Space Physics Data Facility's OMNIWeb service, and OMNI data. The authors thank I. R. Mann, D. K. Milling and the rest of the CARISMA team for data. The AU, AL and SYM-H indices used in this paper were provided by the WDC for Geomagnetism, Kyoto (http://wdc.kugi.kyoto-u.ac.jp/wdc/Sec3.html) via OMNIWeb. CARISMA is operated by the University of Alberta, funded by the Canadian Space Agency; CARISMA data were obtained from http://carisma.ca/carisma-data-repository. SuperMAG is made possible by the generous funding provided by the National Science Foundation (NSF) and National Aeronautics and Space Administration (NASA). We gratefully acknowledge: NSF ATM-0646323, NSF AGS-1003580, NASA NNX08AM32G S03.

The authors acknowledge the use of SuperDARN data. SuperDARN is a collection of radars funded by national scientific funding agencies of Australia, Canada, China, France, Italy, Japan, Norway, South Africa, United Kingdom, and the United States of America. SuperDARN RawACF data were obtained via setting up a user account for the British Antarctic Survey Data mirror (https://www.bas.ac.uk/project/superdarn). Due to the nature of the account setup, data may not be accessible immediately. Support for AMPERE has been provided under NSF sponsorship under Grants ATM-0739864 and AGS-1420184. All AMPERE data are available online (via http://ampere.jhuapl.edu). We thank the AMPERE team and the AMPERE Science Center for providing the Iridium derived data products. The DMSP/SSUSI file type EDR-AUR data were obtained from http://ssusi.jhuapl.edu (data Version 0106, software Version 7.0.0, and calibration period Version E0018). SSUSI is operated under USAF DMSP contract N00024-13-D-6400. This research used the ALICE and SPECTRE High Performance Computing Facility at the University of Leicester. We acknowledge the use of python package PyGeopack which can be downloaded from https://github.com/mattkjames7/PyGeopack.

Acknowledgments

ARF was supported by an STFC studentship, Science Foundation Ireland Grant 18/FRL/6199, and an Irish Research Council Government of Ireland Postdoctoral Fellowship GOIPD/2022/782. ML, TKY, and SEM acknowledge support from the Science and Technology Facilities Council, UKRI, Grant ST/W00089X/1. JAC is supported by Royal Society grant DHF\R1\211068. HKS was supported by an STFC studentship. TE was supported by a Leverhulme Trust Early Career Fellowship (ECF-2019-155), the University of Leicester and the University of Glasgow. SJW was supported by NERC studentship NE/L002493/1. MKJ was supported by STFC Grant ST/W00089X/1. JM-L was supported by the Irish Research Council. LJP was supported by AFOSR MURI Award 26-0201-51-62.

References

Anderson, B., Takahashi, K., Kamei, T., Waters, C., & Toth, B. (2002). Birkeland current system key parameters derived from Iridium observations: Method and initial validation results. *Journal of Geophysical Research: Space Physics*, *107*(A6), 1079. https://doi.org/10.1029/2001JA000080

Anderson, B. J., Korth, H., Waters, C. L., Green, D. L., Merkin, V. G., Barnes, R. J., & Dyrud, L. P. (2014). Development of large-scale Birkeland currents determined from the Active Magnetosphere and Planetary Electrodynamics Response Experiment. *Geophysical Research Letters*, *41*(9), 3017–3025. https://doi.org/10.1002/2014GL059941

Anderson, B. J., Takahashi, K., & Toth, B. A. (2000). Sensing global Birkeland currents with Iridium® engineering magnetometer data. *Geophysical Research Letters*, *27*(24), 4045–4048. https://doi.org/10.1029/2000GL000094

Araki, T. (1994). A physical model of the geomagnetic sudden commencement. *Geophysical Monograph*, *81*, 183–200. https://doi.org/10.1029/GM081p0183

Araki, T., Fujitani, S., Emoto, M., Yumoto, K., Shiokawa, K., Ichinose, T., et al. (1997). Anomalous sudden commencement on March 24, 1991. *Journal of Geophysical Research*, *102*(A7), 14075–14086. https://doi.org/10.1029/96JA03637

Boudouridis, A. E., Zesta, E., Lyons, L. R., Anderson, P. C., & Lummerzheim, D. (2003). Effect of solar wind pressure pulses on the size and strength of the auroral oval. *Journal of Geophysical Research*, *108*(A4), 8012. https://doi.org/10.1029/2002JA009373

Carter, J. A., Milan, S. E., Fogg, A. R., Paxton, L. J., & Anderson, B. J. (2018). The association of high-latitude dayside aurora with NBZ field-aligned currents. *Journal of Geophysical Research: Space Physics*, *123*(5), 3637–3645. https://doi.org/10.1029/2017JA025082

Carter, J. A., Milan, S. E., Fogg, A. R., Sangha, H., Lester, M., Paxton, L. J., & Anderson, B. J. (2020). The evolution of long-duration cusp spot emission during lobe reconnection with respect to field-aligned currents. *Journal of Geophysical Research: Space Physics*, *125*(7), e2020JA027922. https://doi.org/10.1029/2020JA027922

Chi, P. J., Lee, D.-H., & Russell, C. T. (2006). Tamao travel time of sudden impulses and its relationship to ionospheric convection vortices. *Journal of Geophysical Research*, *111*(A8), A08205. https://doi.org/10.1029/2005JA011578

Chi, P. J., Russell, C. T., Raeder, J., Zesta, E., Yumoto, K., Kawano, H., et al. (2001). Propagation of the preliminary reverse impulse of sudden commencements to low latitudes. *Journal of Geophysical Research*, *106*(A9), 18857–18864. https://doi.org/10.1029/2001JA900071

Chisham, G., Freeman, M. P., Coleman, I. J., Pinnock, M., Hairston, M. R., Lester, M., & Sofko, G. (2004). Measuring the dayside reconnection rate during an interval of due northward interplanetary magnetic field. *Annales Geophysicae*, *22*(12), 4243–4258. https://doi.org/10.5194/angeo-22-4243-2004

Chisham, G., Lester, M., Milan, S. E., Freeman, M. P., Bristow, W. A., Grocott, A., et al. (2007). A decade of the Super Dual Auroral Radar Network (SuperDARN): Scientific achievements, new techniques and future directions. *Surveys in Geophysics*, *28*(1), 33–109. https://doi.org/10.1007/s10712-007-9017-8

Claudepierre, S. G., Hudson, M. K., Lotko, W., Lyon, J. G., & Denton, R. E. (2010). Solar wind driving of magnetospheric ULF waves: Field line resonances driven by dynamic pressure fluctuations. *Journal of Geophysical Research: Space Physics*, *115*(A11), A11202. https://doi.org/10.1029/2010JA015399

Coco, I., Amata, E., Marcucci, M. F., Ambrosino, D., & Shepherd, S. G. (2011). Effects of abrupt variations of solar wind dynamic pressure on the high-latitude ionosphere. *International Journal of Geophysics*, *2011*, 1–8. https://doi.org/10.1155/2011/207514

Coco, I., Amata, E., Marcucci, M. F., Ambrosino, D., Villain, J. P., & Hanuise, C. (2008). The effects of an interplanetary shock on the high-latitude ionospheric convection during an IMF By-dominated period. *Annales Geophysicae*, *26*(9), 2937–2951. https://doi.org/10.5194/angeo-26-2937-2008

Coco, I., Amata, E., Marcucci, M. F., De Laurentis, M., Villain, J. P., Hanuise, C., & Candidi, M. (2005). Effects on SuperDARN HF radar echoes on sudden impulses of solar wind dynamic pressure. *Annales Geophysicae*, *23*(5), 1771–1783. https://doi.org/10.5194/angeo-23-1771-2005

Cowley, S. W. H., & Lockwood, M. (1992). Excitation and decay of solar wind-driven flows in the magnetosphere-ionosphere system. *Annales geophysicae*, *10*(1–2), 103–115.

Coxon, J. C., Milan, S. E., & Anderson, B. J. (2018). A review of Birkeland current research using AMPERE. In A. Keiling, O. Marghitu, & M. Wheatland (Eds.), *Electric currents in geospace and beyond*. American Geophysical Union (AGU). https://doi.org/10.1002/9781119324522.ch16

Crooker, N. U. (1992). Reverse convection. *Journal of Geophysical Research: Space Physics*, *97*(A12), 19363–19372. https://doi.org/10.1029/92JA01532

Davis, T. N., & Sugiura, M. (1966). Auroral electrojet activity index AE and its universal time variations. *Journal of Geophysical Research*, *71*(3), 785–801. https://doi.org/10.1029/JZ071i003p00785

Dungey, J. W. (1961). Interplanetary magnetic field and the auroral zones. *Physical Review Letters*, *6*(2), 47–48. https://doi.org/10.1103/PhysRevLett.6.47

Fogg, A. R. (2021). *SuperDARN observations of high latitude electrodynamics in the terrestrial ionosphere*. (Doctoral dissertation). University of Leicester School of Physics and Astronomy. https://doi.org/10.25392/leicester.data.16621912.v1

Fogg, A. R., Jackman, C. M., Waters, J. E., Bonnin, X., Lamy, L., Cecconi, B., et al. (2022). Wind/WAVES observations of auroral kilometric radiation: Automated burst detection and terrestrial solar wind—Magnetosphere coupling effects. *Journal of Geophysical Research: Space Physics*, *127*(5), e2021JA030209. https://doi.org/10.1029/2021JA030209

Fogg, A. R., Lester, M., Yeoman, T. K., Burrell, A. G., Imber, S. M., Milan, S. E., et al. (2020). An improved estimation of SuperDARN Heppner-Maynard boundaries using AMPERE data. *Journal of Geophysical Research: Space Physics*, *125*(5). https://doi.org/10.1029/2019JA027218

Frey, H. U., Mende, S. B., Immel, T. J., Fuselier, S. A., Claflin, E. S., Gérard, J. C., & Hubert, B. (2002). Proton aurora in the cusp. *Journal of Geophysical Research: Space Physics*, *107*(A7), 1091. https://doi.org/10.1029/2001JA900161

Fujita, S., Tanaka, T., Kikuchi, T., Fujimoto, K., Hosokawa, K., & Itonaga, M. (2003). A numerical simulation of the geomagnetic sudden commencement: 1. Generation of the field-aligned current associated with the preliminary impulse. *Journal of Geophysical Research*, *108*(A12), 1416. https://doi.org/10.1029/2002JA009407

Gillies, D. M., St. Maurice, J. P., McWilliams, K. A., & Milan, S. (2012). Global-scale observations of ionospheric convection variation in response to sudden increases in the solar wind pressure. *Journal of Geophysical Research: Space Physics*, *117*(A4). https://doi.org/10.1029/2011JA017255

Gjerloev, J. W. (2012). The SuperMAG data processing technique. *Journal of Geophysical Research*, *117*(A9), A09213. https://doi.org/10.1029/2012JA017683

Greenwald, R. A., Baker, K. B., Dudeney, J. R., Pinnock, M., Jones, T. B., Thomas, E. C., et al. (1995). DARN/SuperDARN: A global view of the dynamics of high-latitude convection. *Space Science Reviews*, *71*(1–4), 761–796. https://doi.org/10.1007/BF00751350

Grocott, A., Badman, S. V., Cowley, S. W. H., Yeoman, T. K., & Cripps, P. J. (2004). The influence of IMF By on the nature of the nightside high-latitude ionospheric flow during intervals of positive IMF Bz. *Annales Geophysicae*, *22*(5), 1755–1764. https://doi.org/10.5194/angeo-22-1755-2004

Grocott, A., Cowley, S. W. H., & Sigwarth, J. B. (2003). Ionospheric flow during extended intervals of northward but B_Y-dominated IMF. *Annales Geophysicae*, *21*(2), 509–538. https://doi.org/10.5194/angeo-21-509-2003

Grocott, A., Milan, S. E., & Yeoman, T. K. (2008). Interplanetary magnetic field control of fast azimuthal flows in the nightside high-latitude ionosphere. *Geophysical Research Letters*, *35*(8), L08102. https://doi.org/10.1029/2008GL033545

Hori, T., Shinbori, A., Fujita, S., & Nishitani, N. (2015). IMF-By dependence of transient ionospheric flow perturbation associated with sudden impulses: SuperDARN observations. *Earth, Planets and Space*, *67*(1), 190. https://doi.org/10.1186/s40623-015-0360-6

Hughes, W. J., & Southwood, D. J. (1976). The screening of micropulsation signals by the atmosphere and ionosphere. *Journal of Geophysical Research*, *81*(19), 3234–3240. https://doi.org/10.1029/JA081i019p03234

Hundhausen, A. J. (1995). The solar wind. In M. G. Kivelson & C. T. Russell (Eds.), *Introduction to space physics* (pp. 91–128). Cambridge University Press.

Iijima, T., & Potemra, T. A. (1976a). The amplitude distribution of field-aligned currents at northern high latitudes observed by Triad. *Journal of Geophysical Research*, *81*(13), 2165–2174. https://doi.org/10.1029/JA081i013p02165

Iijima, T., & Potemra, T. A. (1976b). Field-aligned currents in the dayside cusp observed by Triad. *Journal of Geophysical Research*, *81*(34), 5971–5979. https://doi.org/10.1029/JA081i034p05971

Imber, S. M., Milan, S. E., & Hubert, B. (2006). The auroral and ionospheric flow signatures of dual lobe reconnection. *Annales Geophysicae*, *24*(11), 3115–3129. https://doi.org/10.5194/angeo-24-3115-2006

Iyemori, T. (1990). Storm-time magnetospheric currents inferred from mid-latitude geomagnetic field variations. *Journal of Geomagnetism and Geoelectricity*, *42*(11), 1249–1265. https://doi.org/10.5636/jgg.42.1249

Kikuchi, T., Tsunomura, S., Hashimoto, K., & Nozaki, K. (2001). Field-aligned current effects on midlatitude geomagnetic sudden commencements. *Journal of Geophysical Research*, *106*(A8), 15555–15565. https://doi.org/10.1029/2001JA900030

King, J. H., & Papitashvili, N. E. (2005). Solar wind spatial scales in and comparisons of hourly Wind and ACE plasma and magnetic field data. *Journal of Geophysical Research: Space Physics*, *110*(A2), A02104. https://doi.org/10.1029/2004JA010649

Kivelson, M. G., & Southwood, D. J. (1988). Hydromagnetic waves and the ionosphere. *Geophysical Research Letters*, *15*(11), 1271–1274. https://doi.org/10.1029/GL015i011p01271

Lepping, R. P., Acūna, M. H., Burlaga, L. F., Farrell, W. M., Slavin, J. A., Schatten, K. H., et al. (1995). The Wind magnetic field investigation. *Space Science Reviews*, *71*(1–4), 207–229. https://doi.org/10.1007/BF00751330

Lester, M. (2008). SuperDARN: An example of a network approach to geospace science in the twenty-first century. *Journal of Atmospheric and Solar-Terrestrial Physics*, *70*(18), 2309–2323. https://doi.org/10.1016/j.jastp.2008.08.003

Lester, M. (2013). The Super Dual Auroral Radar Network (SuperDARN): An overview of its development and science. *Advances in Polar Science*, *24*(1), 1–11. https://doi.org/10.3724/SP.J.1085.2013.00001

Lester, M., de la Beaujardiere, O., Foster, J. C., Freeman, M. P., Luhr, H., Ruohoniemi, J. M., & Swider, W. (1993). The response of the large scale ionospheric convection pattern to changes in the IMF and substorms: Results from the SUNDIAL 1987 campaign. *Annales Geophysicae*, *11*, 556–571.

Lin, R. P., Anderson, K. A., Ashford, S., Carlson, C., Curtis, D., Ergun, R., et al. (1995). A three-dimensional plasma and energetic particle investigation for the Wind spacecraft. *Space Science Reviews*, *71*(1–4), 125–153. https://doi.org/10.1007/BF00751328

Lockwood, M., & Cowley, S. W. H. (1992). Ionospheric convection and the substorm cycle. In *Proceedings of the international conference on substorms (ICS-1)* (pp. 99–109).

Mann, I. R., Milling, D. K., Rae, I. J., Ozeke, L. G., Kale, A., Kale, Z. C., et al. (2008). The upgraded CARISMA magnetometer array in the THEMIS era. *Space Science Reviews*, *141*(1–4), 413–451. https://doi.org/10.1007/s11214-008-9457-6

Milan, S. E. (2013). Modeling Birkeland currents in the expanding/contracting polar cap paradigm. *Journal of Geophysical Research: Space Physics*, *118*(9), 5532–5542. https://doi.org/10.1002/jgra.50393

Milan, S. E., Bower, G. E., Carter, J. A., Paxton, L. J., Anderson, J., & Hairston, M. R. (2022). Lobe reconnection and cusp-aligned auroral arcs. *Journal of Geophysical Research: Space Physics*, *127*(6), e2021JA030089. https://doi.org/10.1029/2021JA030089

Milan, S. E., Lester, M., Cowley, S. W. H., & Brittnacher, M. (2000). Dayside convection and auroral morphology during an interval of northward interplanetary magnetic field. *Annales Geophysicae*, *18*(4), 436–444. https://doi.org/10.1007/s00585-000-0436-9

Milan, S. E., Lester, M., Cowley, S. W. H., Oksavik, K., Brittnacher, M., Greenwald, R. A., et al. (2003). Variations in the polar cap area during two substorm cycles. *Annales Geophysicae*, *21*(5), 1121–1140. https://doi.org/10.5194/angeo-21-1121-2003

Milan, S. E., Provan, G., & Hubert, B. (2007). Magnetic flux transport in the Dungey cycle: A survey of dayside and nightside reconnection rates. *Journal of Geophysical Research: Space Physics*, *112*(A1). https://doi.org/10.1029/2006JA011642

Nishitani, N., Ruohoniemi, J. M., Lester, M., Baker, J. B. H., Koustov, A. V., Shepherd, S. G., et al. (2019). Review of the accomplishments of mid-latitude Super Dual Auroral Radar Network (SuperDARN) HF radars. *Progress in Earth and Planetary Science*, *6*(27), 27. https://doi.org/10.1186/s40645-019-0270-5

Ogilvie, K. W., Chornay, D. J., Fritzenreiter, R. J., Hunsaker, F., Keller, J., Lobell, J., et al. (1995). SWE, a comprehensive plasma instrument for the wind spacecraft. *Space Science Reviews*, *71*(1–4), 55–75. https://doi.org/10.1007/BF00751326

Oliveira, D. M., & Raeder, J. (2014). Impact angle control of interplanetary shock geoeffectiveness. *Journal of Geophysical Research: Space Physics*, *119*(10), 8188–8201. https://doi.org/10.1002/2014JA020275

Ozturk, D. S., Zou, S., & Slavin, J. A. (2017). IMF By effects on ground magnetometer response to increased solar wind dynamic pressure derived from global MHD simulations. *Journal of Geophysical Research: Space Physics*, *122*(5), 5028–5042. https://doi.org/10.1002/2017JA023903

Paxton, L. J., Meng, C. I., Fountain, G. H., Ogorzalek, B. S., Darlington, E. H., Gary, S. A., et al. (1992). Special sensor ultraviolet spectrographic imager: An instrument description. In S. Chakrabarti & A. B. Christensen (Eds.), *Instrumentation for planetary and terrestrial atmospheric remote sensing* (Vol. 1745, pp. 2–15). SPIE. https://doi.org/10.1117/12.60595

Redmon, R. J., Denig, W. F., Kilcommons, L. M., & Knipp, D. J. (2017). New DMSP database of precipitating auroral electrons and ions. *Journal of Geophysical Research: Space Physics*, *122*(8), 9056–9067. https://doi.org/10.1002/2016JA023339

Ruohoniemi, J. M., & Baker, K. B. (1998). Large-scale imaging of high-latitude convection with Super Dual Auroral Radar Network HF radar observations. *Journal of Geophysical Research: Space Physics*, *103*(A9), 20797–20811. https://doi.org/10.1029/98JA01288

Shue, J. H., Chao, J. K., Fu, H. C., Russell, C. T., Song, P., Khurana, K. K., & Singer, H. J. (1997). A new functional form to study the solar wind control of the magnetopause size and shape. *Journal of Geophysical Research: Space Physics*, *102*(A5), 9497–9511. https://doi.org/10.1029/97JA00196

Shue, J. H., Song, P., Russell, C. T., Steinberg, J. T., Chao, J. K., Zastenker, G., et al. (1998). Magnetopause location under extreme solar wind conditions. *Journal of Geophysical Research: Space Physics*, *103*(A8), 17691–17700. https://doi.org/10.1029/98JA01103

Smith, A. W., Forsyth, C., Rae, J., Rodger, C. J., & Freeman, M. P. (2021). The impact of sudden commencements on ground magnetic field variability: Immediate and delayed consequences. *Space Weather*, *19*(7), e2021SW002764. https://doi.org/10.1029/2021SW002764

Southwood, D. J. (1974). Some features of field line resonances in the magnetosphere. *Planetary and Space Science*, *22*(3), 483–491. https://doi.org/10.1016/0032-0633(74)90078-6

Takeuchi, T., Araki, T., Viljanen, A., & Watermann, J. (2002). Geomagnetic negative sudden impulses: Interplanetary causes and polarization distribution. *Journal of Geophysical Research: Space Physics*, *107*(A7), 1096. https://doi.org/10.1029/2001JA900152

Tamao, T. (1964). The structure of three-dimensional hydromagnetic waves in a uniform cold plasma. *Journal of Geomagnetism and Geoelectricity*, *16*(2), 89–114. https://doi.org/10.5636/jgg.16.89

Taylor, J. R., Lester, M., & Yeoman, T. K. (1994). A superposed epoch analysis of geomagnetic storms. *Annales Geophysicae*, *12*(7), 612–624. https://doi.org/10.1007/s00585-994-0612-4

Von Rosenvinge, T. T., Barbier, L. M., Karsch, J., Liberman, R., Madden, M. P., Nolan, T., et al. (1995). The energetic particles: Acceleration, composition, and transport (EPACT) investigation on the wind spacecraft. *Space Science Reviews*, *71*(1–4), 155–206. https://doi.org/10.1007/BF00751329

Waters, C., Anderson, B., Green, D., Korth, H., Barnes, R., & Vanhamäki, H. (2020). Science data products for AMPERE. In M. W. Dunlop & H. Lühr (Eds.), *Ionospheric multi-spacecraft analysis tools: Approaches for deriving ionospheric parameters* (pp. 141–165). Springer International Publishing. https://doi.org/10.1007/978-3-030-26732-2_7

Waters, C. L., Anderson, B. J., & Liou, K. (2001). Estimation of global field aligned currents using the Iridium® system magnetometer data. *Geophysical Research Letters*, *28*(11), 2165–2168. https://doi.org/10.1029/2000GL012725

Weimer, D. R., & King, J. H. (2008). Improved calculations of interplanetary magnetic field phase front angles and propagation time delays. *Journal of Geophysical Research: Space Physics*, *113*(A1). https://doi.org/10.1029/2007JA012452

Weimer, D. R., Ober, D. M., Maynard, N. C., Burke, W. J., Collier, M. R., McComas, D. J., et al. (2002). Variable time delays in the propagation of the interplanetary magnetic field. *Journal of Geophysical Research: Space Physics*, *107*(A8), SMP2-91–SMP29-15. https://doi.org/10.1029/2001JA009102

Weimer, D. R., Ober, D. M., Maynard, N. C., Collier, M. R., McComas, D. J., Ness, N. F., & Watermann, J. (2003). Predicting interplanetary magnetic field (IMF) propagation delay times using the minimum variance technique. *Journal of Geophysical Research: Space Physics*, *108*(A1), 1026. https://doi.org/10.1029/2002JA009405

Wilson, L. B., III, Brosius, A. L., Gopalswamy, N., Nieves-Chinchilla, T., Szabo, A., Hurley, K., et al. (2021). A quarter century of wind spacecraft discoveries. *Reviews of Geophysics*, *59*(2), e2020RG000714. https://doi.org/10.1029/2020RG000714

World Data Center for Geomagnetism Kyoto, Nose, M., Iyemori, T., Sugiura, M., & Kamei, T. (2015). Geomagnetic AE index. https://doi.org/10.17593/15031-54800

Wright, A. N., & Elsden, T. (2020). Simulations of MHD wave propagation and coupling in a 3-D magnetosphere. *Journal of Geophysical Research: Space Physics*, *125*(2), e2019JA027589. https://doi.org/10.1029/2019JA027589

Yeoman, T. K., Lester, M., Orr, D., & Lühr, H. (1990). Ionospheric boundary conditions of hydromagnetic waves: The dependence on azimuthal wavenumber and a case study. *Planetary and Space Science*, *38*(10), 1315–1325. https://doi.org/10.1016/0032-0633(90)90134-C

Zuo, P., Feng, X., Xie, Y., Wang, Y., & Xu, X. (2015). Strong solar wind dynamic pressure pulses: Interplanetary sources and their impacts on geosynchronous magnetic fields. *The Astrophysical Journal*, *812*(2), 152. https://doi.org/10.1088/0004-637X/812/2/152